



OPEN

SUBJECT AREAS:

ELECTRICAL AND
ELECTRONIC
ENGINEERINGELECTRONIC AND SPINTRONIC
DEVICES

Evaluation of mobility in thin Bi_2Se_3 Topological Insulator for prospects of Local Electrical Interconnects

Gaurav Gupta, Mansoor Bin Abdul Jalil & Gengchiao Liang

Department of Electrical and Computer Engineering, National University of Singapore, Singapore 117576.

Received
24 June 2014Accepted
10 October 2014Published
30 October 2014Correspondence and
requests for materials
should be addressed to
G.G. (a0089293@
nus.edu.sg) or G.L.
(elelg@nus.edu.sg)

Three-dimensional (3D) topological insulator (TI) has been conjectured as an emerging material to replace copper (Cu) as an interconnect material because of the suppression of elastic scattering from doping and charge impurities for carrier transport on TI surface. We, therefore via full real-space simulation, examine the feasibility of using thin 3D-TI (Bi_2Se_3) wire for the local electrical interconnects in the presence of edge roughness, vacancies, acoustic phonons and charge impurities across temperature and Fermi-level by simulating quantum transport through Non-Equilibrium Green Function algorithm. We found that because of the scattering induced by the acoustic phonons, the mobility reduces considerably at the room temperature which complemented with the low density of states near Dirac-point does not position Bi_2Se_3 3D-TI as a promising material to replace Cu for local interconnects. Properties required in suitable TI material for this application have also been discussed.

Three-dimensional (3D) topological insulator (TI) is a recently¹ discovered material which exhibits gapless topological insulating electronic phase² on its surface and an insulating phase in its bulk. The spin-orbit interaction in 3D-TI results in the band inversion² for the surface bands and serves as important criteria for the search of new 3D-TIs. Among these, Bi_2Se_3 ³ has been the most extensively examined for experimental and theoretical studies owing to its relatively larger bulk bandgap (~ 0.3 eV) that provides greater isolation of surface states from trivial bulk states compared to other TI materials. The fermions on the surface states of 3D-TI have their spins locked to their momentum ensuing chiral spin-texture which protects electrons from backscattering⁴. This atypical material, therefore, warrants investigation of new quantum phenomenon for applications in spintronics⁵⁻⁷. Furthermore, in a Very-Large-Scale Integration (VLSI) circuit, functional blocks communicate data and share clock, ground and power signals among them through a network of wiring system called interconnects, whose bandwidth, dimensions and current carrying capability depends on the signal to be propagated. Due to the suppression of backscattering, TI has been proposed to be a future interconnect material⁸, as a replacement for copper (Cu)⁹ for thickness greater than 5 nm because a five quintuple layer³ (QL) thick sample (~ 4.7 nm) is still a 2D-TI¹⁰⁻¹³ in which the edge-transport severely limits the current carrying capability of the wire. A 6-layer thick Bi_2Se_3 sample (~ 5.658 nm (see Fig. 1(a))) marks the transition to the 3D limit¹⁰, and beyond 10 QL beyond which coupling between the surface-state wavefunction of the top and bottom surfaces becomes sufficiently weak¹⁴ and the sample should, therefore, evince the above-stated topological properties. These propositions are, however, based purely on the electrical and spin properties (spin-momentum locking) of the surface states and neglect the interactions and the role of intermediate bulk layers. As a result, there is a clear need to scrutinize the feasibility and limits of the proposals by modeling real-space quantum transport through 3D-TI wire (c.f. Fig. 1(b)), accounting for all layers and the realistic effects including acoustic phonons and defects.

In this work, the electron mobility in 10 QL to 13 QL thick Bi_2Se_3 3D-TI wire has been comprehensively examined to evaluate its prospects for the electrical interconnect application. Quantum transport through Bi_2Se_3 TI-wire of dimensions suggested for local interconnects was modeled across a range of temperature, and Fermi-level in the presence of edge roughness, vacancies, acoustic phonons and charge impurities within the scope of experimental concentrations. The results show that for the electrical interconnects there is a considerable degradation of mobility at the room temperature due to phonons, even though mobility is relatively robust to other defects. Therefore, the trade-off to gain mobility by operating in topologically protected surface states which inherently have low density of states (DOS) is not very promising for interconnect application, at least at the room temperature. The rest of the paper is organized as follows: in methods section, the simulation approach has been elaborated. In this section, the Hamiltonian required to model a full real-space transport through Bi_2Se_3 TI has

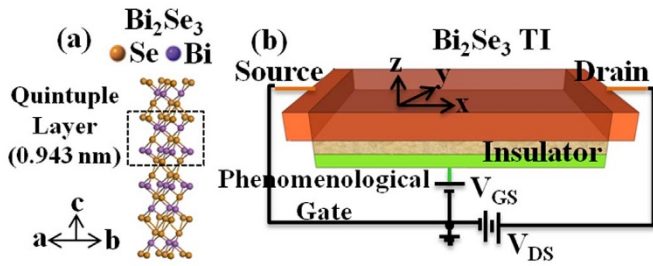


Figure 1 | (a) Atomic structure of Bi_2Se_3 (3D-TI). (b) Device Structure for quantum transport modeling through Bi_2Se_3 nanowire.

been presented along with the key aspects of NEGF in context of this problem. Since, a relatively new computational platform has been used for simulating large wire dimensions in this work; methods section also presents its justification and usefulness for solving such problems. Next, in results section, the important scattering mechanisms, which affect the electron transport through the interconnect wire, are discussed. The evaluation of Bi_2Se_3 TI for interconnect application has been subsequently analyzed in discussion section. Finally, our key findings have been summarized in conclusion section. Section S1 to S3 of the supplementary material with this work has illustrations to help the reader develop more intuitive understanding of results discussed in this paper. Section S4 has the corrected results for some of our related previous work¹⁵.

Methods

This section elaborates three key ingredients of the methodology deployed for modelling a Bi_2Se_3 wire for the study of interconnects. Firstly, the Hamiltonian used to model the quantum transport through the Bi_2Se_3 wires is expounded. Then the non-equilibrium green function (NEGF) formalism¹⁶ (algorithm) for modelling has been summarized. Finally, the computational platform for simulating large interconnects wire has been briefly described.

For the Hamiltonian, each layer of Bi_2Se_3 was originally described in p_z orbital basis in k_p model by H_p (c.f. eq. (1)) as detailed in Ref. 17.

$$H_p = \begin{bmatrix} k^2/m_1 & d+k^2/m_2 & ivk_x - vk_y & 0 \\ d+k^2/m_2 & k^2/m_1 & 0 & -ivk_x + vk_y \\ -ivk_x - vk_y & 0 & k^2/m_1 & d+k^2/m_2 \\ 0 & ivk_x + vk_y & d+k^2/m_2 & k^2/m_1 \end{bmatrix} \quad (1)$$

where $v = 2.5 \text{ eV } \text{\AA}^{-1}$ is the Fermi velocity, $m_1 = 0.125 \text{ eV}^{-1} \text{\AA}^{-2}$ and $m_2 = -0.04 \text{ eV}^{-1} \text{\AA}^{-2}$ are the orbital masses and the parameter $d = -0.22 \text{ eV}$ is introduced to generate a gap. The hopping between adjacent layers was described by tight-binding parameter $t_z = 0.35 \text{ eV}$ in hopping matrix T as per eq. (2).

$$T = \begin{bmatrix} 0 & 0 & 0 & 0 \\ t_z & 0 & 0 & 0 \\ 0 & 0 & 0 & 0 \\ 0 & 0 & t_z & 0 \end{bmatrix} \quad (2)$$

which therefore models Bi_2Se_3 TI in block-tridiagonal form as per eq. (3).

$$H_T = \begin{bmatrix} H_1 & T_1 & & 0 \\ T_1^\dagger & H_2 & T_2 & \\ & T_2^\dagger & H_3 & \\ 0 & & & \end{bmatrix} \quad (3)$$

where $H_1 = H_2 = H_3 = H_p$ and $T_1 = T_2 = T$. The Dirac bands, bulk bandgap and spin-texture for semi-infinite Bi_2Se_3 TI were verified in Fig. 1 of Ref. 17. For modeling the transport in the x -direction for a TI wire of finite width in the y -direction (c.f. Fig. 1(a)), k_x and k_y ($k_x^2 + k_y^2 = k^2$) wave-vectors in eq. (2) were discretized via finite difference method (FDM) by substituting k_m by $-i\nabla_m$.

The energy bands for 3D-TI wire of finite width are plotted in Fig. 2(a). In Fig. 2(a), the confinement along transverse direction quantizes the bands and opens up a small bandgap. To validate the topological property of the wire, the local density of states (LDOS) across the 3D-TI layers had been plotted as shown in Fig. 2(b). It is important to ascertain topological behaviour for a nanowire before evaluating transport because strong confinement (finite-size effect) may destroy topological characteristics¹⁸ along with the corresponding touted conductance properties.

In the implementation of the NEGF algorithm, to calculate the contact self-energy, the surface-Green function for the source and drain contacts was converged itera-

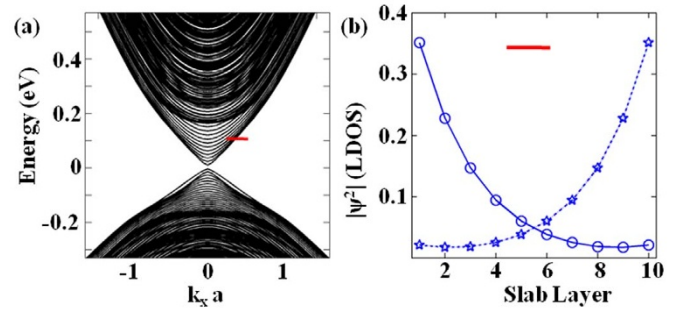


Figure 2 | (a) Energy Bands for 10 QL thick (z -axis) – 60 nm wide (y -axis) Bi_2Se_3 TI nanowire. Small energy bandgap opens due to confinement along y -axis. (b) Local Density of States (LDOS) ($|\psi^2|$) distribution across layers (QLs) of the wire for the first conduction band at the k -point marked with red line in (a). Top and Bottom surfaces can be clearly distinguished from ($|\psi^2|$) distribution which shows localization on the surface layers in accordance with the topological properties. A representative Bi_2Se_3 3D-TI wire of 10 QL thickness – 60 nm width – 80 nm length has been chosen in this work unless specified otherwise.

tively. The device-Green function was evaluated by the recursive-Green function (RGF) algorithm. The acoustic phonon scattering was modeled as a self-energy term¹⁶. For simulating the effect of acoustic phonons in Bi_2Se_3 , the transverse direction (y -axis) was considered in k -space rather than real space, in order to converge the correlation function (G^r in NEGF) in reasonable computational time. However, all other defects in the Bi_2Se_3 wire (vacancies, edge roughness and charge impurities) were modeled in full real-space. The effective mobility from both (phonon and rest of the defects) was then added according to Matthiessen's rule (eq. (4)) to compute the net effect of all contributory factors. The charge correction from Poisson equation had been neglected because of the low-field condition¹⁶.

$$\frac{1}{\mu_{\text{eff}}} = \sum_j \frac{1}{\mu_j} \quad (4)$$

where j includes all effects including ballistic, defect, phonons and so on. In additions, charge (ionic) impurities were modeled as delta-onsite potentials whose position and strength were set via constrained random number generator for a given impurity concentration. We note that a corresponding change in Fermi-level due to the impurities was not accounted because in our model we only consider a phenomenological gate via which we shift the Fermi-level to the same energy value as for the defect-free wire. To model the vacancies, selected lattice points were removed from the Hamiltonian matrix along with all the corresponding interactions in three dimensions. The positions of the vacancies were also regulated by a constrained random number generator. Furthermore, we need to include edge roughness, which originates, e.g., when a sample is cleaved to form a channel, an operation that introduces dangling bonds and vacancies at random lattice sites depending on bond strength at the cleaved interface. The edge roughness was modeled by creating vacancies on the side surfaces i.e. on xz plane in the channel. The 'm%' roughness in simulation results implies that for each sampling point on the wire, for a random number less than 'm' a vacancy was created on the outermost side surface and the one adjacent (inner) to it. For a random number between 'm' and '100-m' a vacancy was created only on the outermost side-surface. Therefore, random number of less than 'm' creates a vacancy defect on the side surface while one greater than '100-m' emulates a dangling bond.

To further validate the model and appropriateness of operation conditions (physical and electronic), non-equilibrium transport current was computed as per eq. (5), and near-equilibrium transport was simulated for a defect-free Bi_2Se_3 wire of 10 QL thickness - 60 nm width and 80 nm length as illustrated in supplementary section S1. The results for random defects were averaged over 25 simulations (refer supplementary Fig. S2.1 for standard deviation for each defect). The effect of these defects on non-equilibrium transport is illustrated in supplementary Fig. S2.2.

$$I_{p \rightarrow q} = \frac{q}{h} \int dE \text{Trace} \left(i \left[H_{pq} G_{qp}^n - G_{pq}^n H_{qp} \right] \right) \quad (5)$$

where 'p' and 'q' are two successive y - z surfaces (sufficiently far from contacts) between which the current was evaluated. The trace was taken for lattice points on the y -axis for each layer. The mobility calculation was described by set of eq. (6) – (13).

$$\text{Green Function: } G^r = [(E + i\eta)I - H_0 - U_0 - \Sigma_S - \Sigma_D - \Sigma_{ph}]^{-1} \quad (6)$$

$$\text{Self-Energy of Phonons: } [\Sigma_{ph}] = D_{ac}[G^r] \quad (7)$$

$$\text{Level Broadening: } \Gamma = i[\Sigma - \Sigma^\dagger] \quad (8)$$



$$\text{Transmission: } \bar{T}(E) = \text{Trace}(\Gamma_S G \Gamma_D G^\vee) \quad (9)$$

$$\text{Density of States [DOS]} = \frac{i}{2\pi} [G^\vee - G^\vee] \quad (10)$$

$$\text{Conductance: } G = \frac{q^2}{h} \int dE \bar{T}(E) \left(-\frac{\partial f}{\partial E} \right) \quad (11)$$

$$\text{Linear Free-Charge Density: } n = \int dE \frac{\text{DOS}(E)}{L} \left(-\frac{\partial f}{\partial E} \right) \quad (12)$$

$$\text{Ballistic Mobility: } \mu = \frac{G \cdot L}{n \cdot q} \quad (13)$$

where subscripts 'S', 'D' and 'ph' refer to source, drain and phonon, respectively, E is a sampling point on the energy grid, D_{ac} is the deformation potential, f is the Fermi-distribution function, L is the length of the wire and other symbols have their usual interpretation. 'n' is charge density in number per unit length. The subsequent evaluation of mobility for interconnects was, however, carried out for near-equilibrium transport to get results across entire temperature range within reasonable computational time.

Next, we introduce the computational platform for modeling large wires for the quantum transport. The presented results in this work are for wires up to 13 layers thick, 63 nm wide (64 sampling points) and 84 nm long (85 sampling points). Therefore, for a sampling distance of 1 nm along the x-y plane with 4x4 basis to describe each point, it corresponds to a unit cell (in the y-z plane of wire) matrix of 3328×3328 size which takes up ~ 169 MB of memory and therefore a *single main-diagonal matrix* for the entire device even with RGF algorithm will take up a huge memory of ~ 14 GB. To surmount the computational challenge of dealing with these large matrices, we had thus resorted to a relatively new hardware in the domain of computational nanoelectronics i.e. General Purpose Graphic Processing Unit (GPGPU). Graphic Processing Units (GPUs) had chiefly remained inaccessible beyond their niche market of video games and some computer science research where algorithms were modeled to emulate the rendering of computer graphics¹⁹ using high-level shading languages like DirectX, OpenGL and Cg. However, lately with the advent of Fermi²⁰ GPU architecture, C enabled software architecture (Compute Unified Device Architecture (CUDA)) and cheap availability of high end Tesla GPUs from Nvidia with hundreds of cores targeted for general purpose scientific computing, GPGPUs have recently been examined for simulating quantum transport for realistic device dimensions²¹. The promising results had been subsequently reported in all the publications. In this work therefore the transport was modeled on Nvidia GPGPU (Tesla C2070 and M2090) in CUDA 5.0 supported by MAGMA 1.3 (Matrix Algebra on GPU and Multicore Architectures) and LAPACK 3.2.1 (Linear Algebra Package) libraries. Specifically, we had optimized the RGF algorithm for memory and speed by breaking up the computation along the channel length to fit into 6 GB GDDR5 RAM of Tesla, and to compute without forming a device diagonal. (The problem would be otherwise unsolvable if full inversion is deployed). The device dimensions used in this work are therefore constrained by the RAM of our computing nodes, but the code is readily scalable to solve much larger devices.

Results

Defect Scattering. The helical Dirac surface states which arise due to strong spin-orbit coupling (SOC) and subsequent band inversion in Bi_2Se_3 topological insulator (a strong-TI) are protected by the time-reversal symmetry (TRS), i.e. $\hat{H}(-\mathbf{k}) = -\hat{H}(\mathbf{k})$. The existence of a single-Dirac cone on the surface prohibits backscattering for perturbations, like non-magnetic charge impurities and vacancies, which cannot break TRS. The odd number of spin-half electrons for surface bands should, however, obey Kramer's degeneracy²². In concurrence to this theorem, it is construed that the bands from top and bottom surface are degenerate but with opposite helicity i.e. they have counter-clockwise and clockwise spin-texture²³ on top and bottom surface, respectively. If the thickness of TI is very small, the wavefunction of the two surfaces can overlap (inter-surface coupling or crosstalk) and therefore the electron in the forward moving state of one surface can backscatter into the backward moving state of the other surface. For a sufficiently thick TI with negligible crosstalk, the surface transport in principle should be immune to the charge impurities and vacancies.

This theoretical assertion is, however, based on a semi-classical scattering picture for momentum conserved interaction (elastic process) of electrons with defects and overlooks other aspects of electronic interaction with defects in a device²⁴. Vacancies, for

example, can induce trap states in the bulk bandgap of TI²⁵ and charge impurities may affect the carrier transport by scattering the electrons to bulk layers²⁶ or by creating a localized resonant state^{27,28} that even though does not destroy the Dirac-point (locally), can significantly modify the local density of states (LDOS)²⁹. The effect of defects is, however, felt only in the vicinity of the defect²⁷. Therefore, even though the theoretical²⁸ and experimental^{4,27,29,30} examination of the TRS protected surface state for 3D-TI in presence of non-magnetic defects has found it to be robust around the Dirac-point³¹, there is a limit to the robustness depending on the magnitude, density and spatial distribution of the defects. Even if the individual impurity potential is weak but occur in sufficiently high spatial density, then the defects can scatter the electrons and reduce the mobility. Large impurity concentration can also modulate the energy band to drive the topological insulator into a trivial insulating state³², which becomes especially important because of the large defect concentration of vacancies and impurities in freshly prepared samples. Therefore, due to the qualified invulnerability of quantum transport to the elastic scattering mechanisms, the effect of charge impurities and vacancies on carrier mobility deserves scrutiny and has been comprehensively examined over a broad range of concentration in discussion section.

Phonon Scattering. The uniformly packed atoms in a lattice at 0 K start to vibrate like coupled springs as the temperature is increased. The coherent collective motion of these atoms i.e. the acoustic phonons exchange momentum with the electrons to relax the latter's momentum. Since, negligible energy is exchanged in this phenomenon the electrons continue to propagate at the same energy but are forced to change the direction (momentum vector). At non-equilibrium, this may gradually lead to the backscattering of the electrons despite their initial forward moving state. For low non-magnetic defect density, the topologically protected surface states are therefore most vulnerable to acoustic phonon scattering processes¹⁷. The impact of acoustic phonons scales with the temperature and length of the channel which makes this phenomenon even more important for interconnect wires operating at room temperature or even at elevated temperature in packaged integrated circuits. In the most comprehensively studied material Bi_2Se_3 , the strength of electron-phonon coupling (λ) although contended over a large range (from 0.08 to 0.43) is still relatively strong³³. At a subtler level, temperature induces two opposing trends –it not only scales the strength of acoustic phonons that make the transport more resistive, but also thermally activates the carriers into higher energy states in accordance to Fermi-Dirac statistics, which usually enhances the conductivity of the material. The energy level broadening induced by the phonon scattering furthermore may aid in the thermal activation depending on the Fermi-level of the system. Since, the Fermi-level of pristine Bi_2Se_3 lies in the bulk conduction bands due to the selenide vacancies, for systems operating without gate control, the most common scheme is to dope with p-type impurities^{34,35} to bring down the Fermi-level closer to the Dirac-point. Therefore, due to the multitude of factors competing or complementing with one another, the prospects of Bi_2Se_3 3D-TI interconnect has been investigated in presence of all defects across temperature and Fermi-level in discussion section for different wire widths and thicknesses.

Discussion

Some of the key properties being sought in a material to replace Cu as the electrical interconnect at the room temperature are high mobility, passivity to edge roughness and defects. Therefore, each of these has been individually examined in Fig. 3, and finally the collective effects of all the defects and phonons have been put together in Fig. 4 and Fig. 5 to appraise the prospects of 3D-TI for interconnects.

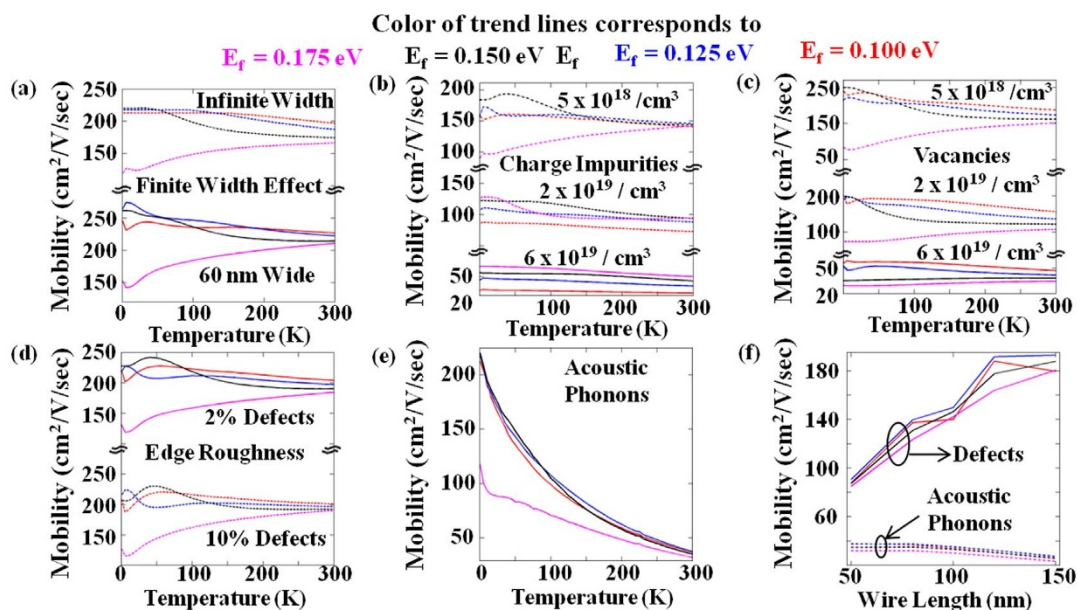


Figure 3 | Mobility characterization across temperature at different Fermi-Levels (E_f). (a) Ballistic Mobility for a finite width and an infinitely wide wire. Effect of charge impurities (b), vacancies (c), edge roughness (d) and acoustic phonon (e) on mobility. (f) Effect of defects (10% Edge Roughness + $5 \times 10^{18}/\text{cm}^3$ Charge Impurities + $5 \times 10^{18}/\text{cm}^3$ vacancies) and phonons on mobility at 300 K with the scaling of the wire length. Note that for low defect concentration mobility trends follow approximately ballistic results.

As shown in Fig. 3(a), the confinement due to finite width (also refer supplementary Fig. S1.2) of wire limits the propagation modes, quantizes the surface band and induces a mini-bandgap. The scaling of both DOS and transmission (see eq. (11) – (13)), however, results in approximately the same ballistic mobility values. This shows the robustness of TI to finite width effects which is an important requirement for interconnects. The mobility is also significantly good for interconnects ($\text{Cu} \sim 30 \text{ cm}^2/\text{V}\cdot\text{s}^{36}$). In Fig. 3(b) and Fig. 3(c) charge impurities and vacancies are then considered in a 60 nm-wide wire at experimentally observed concentrations in Bi_2Se_3 ^{37–39}. For premium quality (Se vacancy compensated) Bi_2Se_3 ¹⁴ samples with low defect concentration (good quality samples¹⁴) and operating close to the Dirac point, the mobility is practically immune to charge impurities. It is because non-magnetic impurities do not break time-reversal symmetry on TI surface, and therefore cannot result in backscattering. Moreover, for low defect concentration, as explained in the results section for defect scattering, electron cannot be scattered from defect to defect because of localized influence of defect-site due to

non-overlapping wavefunction of the defects. De facto fabrication of Bi_2Se_3 TI, however, has very high impurity and vacancy concentration³⁷. At large concentrations, the mobility degrades and makes the wire more resistive and less useful as an interconnect-wire. (see supplementary Fig. S2.1 for plots of DOS, transmission and charge distribution and supplementary Fig. S2.2 for current distribution across layers for each type of defect to develop an intuitive understanding of the transport and mobility behaviour in a TI-wire). Similarly, the insensitivity of mobility to edge roughness (c.f. Fig. 3(d)) that results from transport being chiefly through the lateral centre of the wire (along the y-axis) (c.f. supplementary Fig. S2.1) and high thermal conductivity⁴⁰ which is required to circumvent electromigration problems, seemingly qualifies 3D-TI as a good candidate for interconnects. However, as shown in Fig. 3(e), the acoustic phonons substantially reduce the mobility at higher temperatures because of strong electron-phonon coupling. Furthermore, the effect of low defect concentration and phonons on mobility at 300 K has been separately examined in Fig. 3(f) over a wide range of length of local interconnect-wires. As expected, the trend line for the effect of defects is reminiscent of approximately ballistic behaviour (see eq. (13)), whereas phonons can scatter more electrons for longer wire lengths. Furthermore as shown in Fig. 4, the collective effect of all the defects (in real-space) in low-concentration along with phonons (uncoupled transverse modes in k-space) computed via Matthiessen's rule (see eq. (4)) (also see Ref. 41 for detailed technique of adding partial mobilities) successfully emulates the experimentally⁴² observed trends. Specifically, note that phonons dominate the high temperature characteristics of mobility, because the mobility values for wire with phonons are much lower than cases with defects (see eq. (4)). Thereafter, the effect of interconnect wire width and thickness has been examined at room temperature in presence of phonons and other defects as illustrated in Fig. 5. In Fig. 5(a), for a given thickness, although total DOS increases with width, inter-surface coupling is constant. Therefore, for the wire width in topological regime the mobility is approximately constant. We, however, note that in our simulation, this could also be because phonons which have dominant effect on mobility have been evaluated for same (periodic) width and may therefore mask the effect of defects and

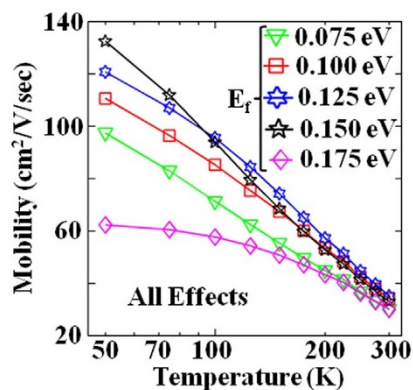


Figure 4 | Effective mobility in presence of all the defects (Phonons + 10% Edge Roughness + $5 \times 10^{18}/\text{cm}^3$ Charge Impurities + $5 \times 10^{18}/\text{cm}^3$ vacancies) as described by Matthiessen's rule (see eq. (4)) for different Fermi-Levels.

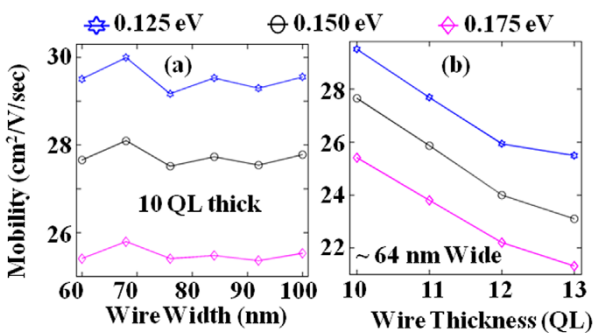


Figure 5 | 80 nm long – 64 nm wide TI-wire at 300 K. (a) Effect of wire width and (b) thickness on the mobility in presence of all the defects (Phonons + 10% Edge Roughness + $5 \times 10^{18}/\text{cm}^3$ Charge Impurities + $5 \times 10^{18}/\text{cm}^3$ vacancies) for different Fermi-Levels at 300 K.

increased DOS for larger widths. To validate this hypothesis, the phonons should be simulated in the same nanowire in real-space which is computationally prohibitive presently and may be addressed in future. Hence, based on the current observations, Bi₂Se₃ TI wire exhibits good robustness to finite width effects. For increased wire thickness the inter-surface coupling should reduce and defect-scattering should become weaker as explained in results section, but DOS increases due to increased number of layers with only a small change in transmission, due to operation in surface bands, resulting in a small decrease in mobility as illustrated in Fig. 5(b).

As a possible future interconnects material, 3D-TI has to compete with other materials among which the major contenders for replacement are single-walled carbon-nanotubes (SW-CNT) and graphene-nano ribbons (GNR). Between these two variants of carbon, recently the later has been more strongly pursued because of relatively simpler fabrication process⁴³. Therefore, we now briefly discuss their properties in order to understand the relative prospects of topological insulators vis-à-vis the above carbon-based competitors. At room-temperature bulk Cu³⁶ has mobility of $\sim 30 \text{ cm}^2/\text{V}\cdot\text{sec}$ and conductivity of $\sim 2.5\text{--}3.3 \times 10^7 (\Omega\text{-m})^{-1}$ (2005 ITRS for 52 nm–90 nm wide Cu wire) (free electron density of $\sim 10^{29}/\text{m}^3$). Copper interconnects for such small wire widths suffer from electromigration effects and grain-boundary scattering (edge effects). The large current densities ($> 10^9 \text{ A}/\text{cm}^2$) without material breakdown can be sustained in GNR by its in-plane strong sp^2 hybridized sigma bonds. Additionally, electromigration is suppressed in GNRs due to their large thermal conductivity⁴⁴, and high momentum relaxation time arising from long mean-free path ($\sim 1 \mu\text{m}$) indeed positions GNR as a good interconnect material. However, the low mode density and low DOS of monolayer GNR interconnect⁴⁵ makes it highly resistive, whereas the electron mobility is degraded because of the inter-layer coupling in multi-layer GNR (MLGNR). Therefore, a prospective solution⁴⁶ is to consider an intercalated zigzag edged MLGNR (side-contacts) of high specularity ($p \sim 1$) and of sufficient inter-layer separation. On the other hand, even though single SWCNT also suffer from low DOS problem, they can be bundled⁴⁷ together to enhance their performance. For more detailed discussion on prospects of these two materials as a replacement of Cu, the reader is referred to a recent review article⁴⁸.

To induce topological protection from elastic scattering in 3D-TI, Fermi-level should be close to the Dirac-point. The DOS is considerably low around Dirac-point compared to large mode density in Cu at Fermi-level, and in fact tends to zero at the Dirac-point. The low DOS corresponds to bulk carrier density of $\sim 10^{23}/\text{m}^3$ ³⁸ and conductivity even at low-temperature ($\sim 2\text{K}$) lies in the range of only $8.9\text{--}34.5 \times 10^3 (\Omega\text{-m})^{-1}$ ³⁴. However, to the best of our knowledge, no multi-layer stacks or bundles, or any such technique to exploit mul-

iple 3D-TI channels exists to substantially increase the conductivity while operating close to the Dirac-point. Therefore, even though at low-temperatures 3D-TI has experimentally shown high mobility³⁵, at the room temperature the topologically protected surface states exhibit low mobility due to acoustic phonons, coupled with their low DOS.

Conclusion

Although the topological surface states of 3D-TIs have high mobility at low temperature ($\sim 2 \text{ K}$) and are immune to edge roughness, charge impurities and vacancies in reasonable concentrations, the mobility is significantly lower at room temperature due to acoustic phonon scattering. Therefore, the trade-off to gain mobility by operating in topologically protected surface states, with inherently low Density of States (DOS) near the Dirac-point, is not encouraging enough to suggest thin Bi₂Se₃ 3D-TI as a good candidate for the replacement of Cu as the local interconnects material especially at the room temperature. However, we note that some other 3D-TI material with large bandgap, for greater isolation between high-mobility topologically protected surface with bulk layers⁴⁹, and weak acoustic phonon scattering may still be a good contender for interconnect wires. It is also noted that very thick Bi₂Se₃ 3D-TI may exhibit large mobility as shown in a recent experimental work³⁰, which implies that for applications where thick interconnects are permissible 3D-TI may be a viable option, and an interesting possibility for future investigation. Other possible alternative is to experimentally devise innovative schemes like to bundle or have stacks of 3D-TI which may improve their electrical properties for interconnects.

1. Fu, L., Kane, C. L. & Mele, E. J. Topological insulators in three dimensions. *Phys. Rev. Lett.* **98**, 106803 (2007).
2. Hasan, M. Z. & Kane, C. L. Colloquium: Topological insulators. *Rev. Mod. Phys.* **82**, 3045–3067 (2010).
3. Xia, Y. *et al.* Observation of a large-gap topological-insulator class with a single Dirac cone on the surface. *Nat. Phys.* **5**, 398–402 (2009).
4. Roushan, P. *et al.* Topological surface states protected from backscattering by chiral spin texture. *Nature* **460**, 1106–1109 (2009).
5. Pesin, D. & MacDonald, A. H. Spintronics and pseudospintronics in graphene and topological insulators. *Nat. Mater.* **11**, 409–416 (2012).
6. Yan, Y. *et al.* Topological Surface State Enhanced Photothermoelectric Effect in Bi₂Se₃ Nanoribbons. *Nano Lett.* **14**, 4389–4394 (2014).
7. Gupta, G., Jalil, M. B. A. & Liang, G. Effect of Band-Alignment Operation on Carrier Transport in Bi₂Se₃ Topological Insulator. *Sci. Rep.* **4**, 6220 (2014).
8. Zhang, X. & Zhang, S. C. Chiral interconnects based on topological insulators. *Micro- and Nanotech. Sens., Sys., and App. IV* **8373**, 837309 (2012).
9. The International Technology Roadmap for Semiconductors (ITRS), *Interconnects* (2011). Available at: <http://www.itrs.net/>. [Date of access: 01/06/2013].
10. Zhang, Y. *et al.* Crossover of the three-dimensional topological insulator Bi₂Se₃ to the two-dimensional limit. *Nat. Phys.* **6**, 584–588 (2010).
11. Kane, C. L. & Mele, E. J. Quantum spin Hall effect in graphene. *Phys. Rev. Lett.* **95**, 226801 (2005).
12. Qiao, Z., Tse, W.-K., Jiang, H., Yao, Y. & Niu, Q. Two-Dimensional Topological Insulator State and Topological Phase Transition in Bilayer Graphene. *Phys. Rev. Lett.* **107**, 256801 (2011).
13. Knez, I., Du, R.-R. & Sullivan, G. Evidence for Helical Edge Modes in Inverted InAs/GaSb Quantum Wells. *Phys. Rev. Lett.* **107**, 136603 (2011).
14. Kim, D. *et al.* Surface conduction of topological Dirac electrons in bulk insulating Bi₂Se₃. *Nat. Phys.* **8**, 458–462 (2012).
15. Gupta, G., Jalil, M. B. A. & Liang, G. Is sub-10nm thick 3D-topological insulator good for the local electrical interconnects? *IEEE Internat. Elec. Dev. Meet. (IEDM)* 32.5.1–32.5.4 (2013).
16. Datta, S. *Lessons from Nanoelectronics: A New Perspective on Transport*. (World Scientific Publishing Company Incorporated, Singapore, 2012).
17. Gupta, G., Lin, H., Bansil, A., Jalil, M. B. A. & Liang, G. Role of acoustic phonons in Bi₂Se₃ topological insulator slabs: A quantum transport investigation. *Phys. Rev. B* **89**, 245419 (2014).
18. Zhou, B., Lu, H.-Z., Chu, R.-L., Shen, S.-Q. & Niu, Q. Finite Size Effects on Helical Edge States in a Quantum Spin-Hall System. *Phys. Rev. Lett.* **101**, 246807 (2008).
19. Sanders, J. & Kandrot, E. *CUDA by Example: An Introduction to General-Purpose GPU Programming*. (Addison-Wesley Professional, United States of America, 2010).



20. NVIDIA's Next Generation CUDA Compute Architecture: Fermi. *Nvidia Whitepaper*, (2007). Date of access: 05/02/2013.
21. Ihnatsenka, S. Computation of electron quantum transport in graphene nanoribbons using GPU. *Comput. Phys. Commun.* **183**, 543–546 (2012).
22. Bardarson, J. H. A proof of the Kramers degeneracy of transmission eigenvalues from antisymmetry of the scattering matrix. *J. Phys. a-Math. Theor.* **41**, 405203 (2008).
23. Hsieh, D. *et al.* Observation of Unconventional Quantum Spin Textures in Topological Insulators. *Science* **323**, 919–922 (2009).
24. Ran, Y., Zhang, Y. & Vishwanath, A. One-dimensional topologically protected modes in topological insulators with lattice dislocations. *Nat. Phys.* **5**, 298–303 (2009).
25. Shan, W. Y., Lu, J., Lu, H. Z. & Shen, S. Q. Vacancy-induced bound states in topological insulators. *Phys. Rev. B* **84**, 035307 (2011).
26. Chan, C. & Ng, T. K. Impurity scattering in the bulk of topological insulators. *Phys. Rev. B* **85**, 115207 (2012).
27. Teague, M. L. *et al.* Observation of Fermi-energy dependent unitary impurity resonances in a strong topological insulator Bi₂Se₃ with scanning tunneling spectroscopy. *Solid State Commun.* **152**, 747–751 (2012).
28. Black-Schaffer, A. M. & Balatsky, A. V. Subsurface impurities and vacancies in a three-dimensional topological insulator. *Phys. Rev. B* **86**, 115433 (2012).
29. Alpichshev, Z. *et al.* STM Imaging of Impurity Resonances on Bi₂Se₃. *Phys. Rev. Lett.* **108**, 206402 (2012).
30. Zhang, T. *et al.* Experimental Demonstration of Topological Surface States Protected by Time-Reversal Symmetry. *Phys. Rev. Lett.* **103**, 266803 (2009).
31. Alpichshev, Z. *et al.* STM Imaging of Electronic Waves on the Surface of Bi₂Te₃: Topologically Protected Surface States and Hexagonal Warping Effects. *Phys. Rev. Lett.* **104**, 016401 (2010).
32. Wu, L. *et al.* A sudden collapse in the transport lifetime across the topological phase transition in (Bi_{1-x}In_x)₂Se₃. *Nat. Phys.* **9**, 410–414 (2013).
33. Giraud, S., Kundu, A. & Egger, R. Electron-phonon scattering in topological insulator thin films. *Phys. Rev. B* **85**, 035441 (2012).
34. Hong, S. S., Cha, J. J., Kong, D. S. & Cui, Y. Ultra-low carrier concentration and surface-dominant transport in antimony-doped Bi₂Se₃ topological insulator nanoribbons. *Nat. Commun.* **3**, 757 (2012).
35. Wei, P., Wang, Z. Y., Liu, X. F., Aji, V. & Shi, J. Field-effect mobility enhanced by tuning the Fermi level into the band gap of Bi₂Se₃. *Phys. Rev. B* **85**, 201402(R) (2012).
36. Suri, R., Thakoor, A. P. & Chopra, K. L. Electron-Transport Properties of Thin Copper-Films. *J. Appl. Phys.* **46**, 2574–2582 (1975).
37. Cao, H. L. *et al.* Structural and electronic properties of highly doped topological insulator Bi₂Se₃ crystals. *Phys. Status Solidi-R* **7**, 133–135 (2013).
38. Kim, D., Syers, P., Butch, N. P., Paglione, J. & Fuhrer, M. S. Coherent topological transport on the surface of Bi₂Se₃. *Nat. Commun.* **4**, 2040 (2013).
39. Xiu, F. X. *et al.* Quantum Capacitance in Topological Insulators. *Sci. Rep.* **2**, 669; DOI:10.1038/srep00669 (2012).
40. Hor, Y. S. *et al.* p-type Bi₂Se₃ for topological insulator and low-temperature thermoelectric applications. *Phys. Rev. B* **79**, 195208 (2009).
41. Niquet, Y.-M. *et al.* Quantum calculations of the carrier mobility: Methodology, Matthiessen's rule, and comparison with semi-classical approaches. *J. Appl. Phys.* **115**, 054512 (2014).
42. Zhu, H. *et al.* Topological Insulator Bi₂Se₃ Nanowire High Performance Field-Effect Transistors. *Sci. Rep.* **3**, 1757; DOI:10.1038/srep01757 (2013).
43. Behnam, A. *et al.* Transport in Nanoribbon Interconnects Obtained from Graphene Grown by Chemical Vapor Deposition. *Nano Lett.* **12**, 4424–4430 (2012).
44. Balandin, A. A. *et al.* Superior thermal conductivity of single-layer graphene. *Nano Lett.* **8**, 902–907 (2008).
45. Naeemi, A. & Meindl, J. D. Conductance modeling for graphene nanoribbon (GNR) interconnects. *IEEE Elec. Dev. Lett.* **28**, 428–431 (2007).
46. Xu, C. A., Li, H. & Banerjee, K. Modeling, Analysis, and Design of Graphene Nano-Ribbon Interconnects. *IEEE Trans. Elec. Dev.* **56**, 1567–1578 (2009).
47. Kureshi, A. K. & Hasan, M. Analysis of CNT Bundle and Its Comparison with Copper Interconnect for CMOS and CNFET Drivers. *J. Nanomater.* **2009**, 486979 (2009).
48. Rakheja, S., Kumar, V. & Naeemi, A. Evaluation of the Potential Performance of Graphene Nanoribbons as On-Chip Interconnects. *Proc. IEEE* **101**, 1740–1765 (2013).
49. Tanaka, Y. *et al.* Experimental realization of a topological crystalline insulator in SnTe. *Nat. Phys.* **8**, 800–803 (2012).
50. Yan, Y. *et al.* High-Mobility Bi₂Se₃ Nanoplates Manifesting Quantum Oscillations of Surface States in the Sidewalls. *Sci. Rep.* **4**, 3817; DOI:10.1038/srep03817 (2014).

Acknowledgments

The work at the National University of Singapore was supported by MOE under Grant No. R263000689112 and MOE2013-T2-2-125. This work benefited from the allocation of time at the High-Performance Computing Gold Cluster for GPGPU simulations. M.B.A.J. acknowledges the Singapore National Research Foundation for support under NRF-CRP9-2011-01.

Author contributions

G.G. performed the computations and wrote the manuscript. G.G., M.B.A.J. and G.L. critically analyzed the data. All authors reviewed the manuscript. G.L. also managed the overall execution of the project.

Additional information

Supplementary information accompanies this paper at <http://www.nature.com/scientificreports>

Competing financial interests: The authors declare no competing financial interests.

How to cite this article: Gupta, G., Jalil, M.B.A. & Liang, G. Evaluation of mobility in thin Bi₂Se₃ Topological Insulator for prospects of Local Electrical Interconnects. *Sci. Rep.* **4**, 6838; DOI:10.1038/srep06838 (2014).



This work is licensed under a Creative Commons Attribution-NonCommercial-ShareAlike 4.0 International License. The images or other third party material in this article are included in the article's Creative Commons license, unless indicated otherwise in the credit line; if the material is not included under the Creative Commons license, users will need to obtain permission from the license holder in order to reproduce the material. To view a copy of this license, visit <http://creativecommons.org/licenses/by-nc-sa/4.0/>